Physics of Plasmas ARTICLE scitation.org/journal/php

Gyrokinetic simulations of m = 0 mode in sheared flow Z-pinch plasmas

Cite as: Phys. Plasmas **26**, 062114 (2019); doi: 10.1063/1.5100542
Submitted: 17 April 2019 · Accepted: 17 May 2019 ·
Published Online: 17 June 2019

V. I. Geyko, M. Dorf, and J. R. Angus

AFFILIATIONS

Lawrence Livermore National Laboratory, Livermore, California 94550, USA

ABSTRACT

Axisymmetric stability properties of sheared flow Z-pinch plasmas are studied by making use of the gyrokinetic approximation in the long-wavelength limit. Numerical simulations are carried out with the high-order finite-volume code COntinuum Gyrokinetic Edge New Technology (COGENT) and are analyzed for the parameters characteristic of the FuZE experiment. Reduction of the linear growth rate with increasing shear is observed, and the results are elucidated by making use of a local dispersion relation analysis. In addition, COGENT simulations are compared with fully kinetic particle-in-cell simulations, and with an ideal magnetohydrodynamics (MHD) model. Good agreement between the gyrokinetic and fully kinetic results for the linear stability is found, with the gyrokinetic model requiring much less computational time due to its ability to step over particle gyroperiod. The ideal MHD model is found to be consistent with the kinetic models in the long-wavelength part of the spectra ($k\rho_i$), while failing to adequately predict short-scale ($k\rho_i$) stability. Here, k is the axial wavelength vector and ρ_i is the ion gyroradius.

I. INTRODUCTION

A plasma column confined by closed azimuthal magnetic fields, also known as a Z-pinch, has received considerable attention in the last several decades due to its possible applications in fusion energy,[1–4] generation of X-rays and high magnetic fields,[5] and general academic interest.[6] However, such plasma configurations are prone to magneto-hydrodynamics (MHD) instabilities, which develop on fast Alfvén time scales, disrupt the current, and destroy the equilibrium. Among these instabilities, the two notorious ones are the axially symmetric "sausage" $m = 0$ mode and the "kink" mode with $m = 1$ azimuthal number. They have been thoroughly studied in the literature and have been shown to have the highest growth rates.[7]

The interest in Z-pinches was renewed with the recent experiments on sheared-flow stabilized Z-pinches (FSZPs).[8–12] These experiments demonstrated[12] pinch stabilization on a time scale of the order of 5000 r_0/V_a, where r_0 is the characteristic radius of the pinch and V_a is the Alfvén velocity given by $V_a = B_0/\sqrt{4\pi m_i n_i}$, with magnetic field B_0 and density n_i taken at their peak values. The analytical analysis[13] employing an ideal MHD model can predict stabilization of the kink mode by a relatively small shear value of the axial velocity $\partial_r v_z \geq 0.1kV_a$, where k is the wave number of the mode. However, reported values of the axial velocity variation required to stabilize the sausage mode vary from sub-Alfvénic[8] to 1–4 Alfvén speed range.[14–16]

Current experimental realization of flow stabilized Z-pinch (FSZP) systems generates radial variations in the axial flow velocity on the scale of the pinch radius r_0. As such, the sheared flow can smear out and mitigate long wavelength modes, i.e., $kr_0 \leq 1$, but not the short wavelength modes whose spatial scale is much smaller than r_0. In addition to the high-k part of the ideal MHD modes, Z-pinch plasmas can also suffer from short-scale nonideal drift-type instabilities.[7,17–21] They appear in the (nonideal) hydrodynamic description of the Z-pinch system if the drift terms of order ρ_i/r_0 are retained and the heat transfer moment equations for ions and electrons are considered (ρ_i is the ion gyroradius). The distinguishing feature of these modes is that the total ion plus electron pressure remains unperturbed to the leading order for the long-wavelength case $k\rho_i \ll 1$. This means that the total entropy of the system is perturbed—hence the name "entropy mode." Note that the ideal MHD description assumes an adiabatic equation of state and therefore constant entropy.[20] For $k\rho_i \sim 1$, entropy modes have growth rates[18] $\gamma \sim V_a/r_0$, which is on the same scale as the growth rates of the dominant ideal MHD modes. Although the spatial scale for the drift-waves can be much smaller than the pinch size, the corresponding microturbulence can significantly increase the radial transport of the pinch macroquantities. For instance, such enhanced plasma viscosity can rapidly reduce the flow shear beyond the values required for the Z-pinch stability.[22]

For parameters characteristic of the FSZP experiments,[23] the ion collisional frequency is much smaller than the entropy mode frequency, with the possible exception in the pinch edge where the plasma temperature can rapidly decrease[11] and collisional effects (such as gyrorelaxation[20,21]) might need to be included. Therefore, the standard hydrodynamic (fluid) methods are not applicable to study this problem. Furthermore, even though the dynamics of the $m = 0$ (flute) entropy modes occurs only in the perpendicular to magnetic field directions, the so-called perpendicular closures[24] that are used in fluid descriptions of magnetized plasmas in the limit of $k\rho_i \ll 1$ are not applicable for the most unstable $k\rho_i \sim 1$ modes either. We note however various ways that can be used to qualitatively capture $k\rho_i \sim 1$ effects in MHD descriptions. Finite ion Larmor radius effects can be included in hydrodynamic descriptions via terms such as the Hall term,[16,25] diamagnetic heat flux,[7] and the ion-gyroviscous stress tensor.[26] One can find more details on the extended MHD model in the following paper.[27]

Kinetic simulations are able to capture all necessary physics correctly, yet they are too computer resource demanding and therefore cannot be used as a simple tool to analyze the problem. The problem of entropy-mode-driven microturbulence in the FSZP ongoing and planned experiments is, however, ideally suited for the gyrokinetic formalism. Indeed, the time scale of the entropy mode is much longer than the ion cyclotron gyration period, and the ion gyroradius is much smaller than the equilibrium length scales, $\rho_i/r_0 \sim 0.1$ (note that the terms neglected in the gyrokinetic approximation are of the order of ρ_i^2/r_0^2, and therefore are small). It should be mentioned that because the magnetic field goes to zero at the pinch axis, the ions are not "magnetized" and the gyrokinetic formalism breaks down near the axis. However, it is the magnetized edge that is of interest, as both nonlinear simulations[28] and experiments[11] show that a shear located at the edge of the plasma is sufficient to provide stabilization.

In the present work, results are presented from numerical simulations of $m = 0$ modes in the long-wavelength limit performed with the electrostatic gyrokinetic 4D code COGENT (COntinuum Gyrokinetic Edge New Technology). Unlike local gyrokinetic simulations previously done with the GS2 code,[18] the simulations here are global as radial plasma profile variations are retained, though the near-axis unmagnetized region is excluded. We find that the most unstable global mode is localized at approximately the region of the maximum magnetic field, and therefore it is unaffected by the details of the boundary conditions at the inner radial boundary. Even such a simplified model, which presently does not include electromagnetic effects, and only contains finite Larmor radius (FLR) effects as a polarization term in the gyrokinetic Poisson equation (GPE), provides adequate mode behavior and the results are in a good agreement with recent particle-in-cell (PIC) simulations.[29] The reduction of the linear growth rate with increasing shear is observed and the results are elucidated by making use of a local linear dispersion relation analysis.

The paper is organized as follows. The main parameters of the system are defined in Sec. II. This includes the gyrokinetic equations, pinch equilibrium, simulation setup, and computational domain. In Sec. III, a local linear dispersion relation for both entropy and ideal modes is derived from the governing equations. Simulation results are presented in Sec. IV. Linear growth rates are compared with previously reported values from MHD and fully kinetic models. The effects of shear are illustrated. The main results of the paper are summarized in Sec. V, where the applicability of the gyrokinetic equations as well as possible future improvements are also discussed.

II. SIMULATION SETUP

Numerical simulations are performed using the continuum gyrokinetic code COGENT, which utilizes a high-order finite-volume discretization of the electrostatic gyrokinetic equation in 2D2V phase-space. The 2V velocity space dimensions are the parallel velocity and the magnetic moment. For the simulations here, the 2D configuration space is cylindrical with radial and axial coordinates. The code solves the gyrokinetic equation for the distribution function of species α, where $\alpha = \mathrm{i}$ for ions and $\alpha = \mathrm{e}$ for electrons

$$\frac{\partial(B^*_{\parallel\alpha} f_\alpha)}{\partial t} + \nabla_{\mathbf{R}} \cdot \left(\dot{\mathbf{R}}_\alpha B^*_{\parallel\alpha} f_\alpha\right) + \frac{\partial}{\partial v_\parallel}\left(\dot{v}_{\parallel\alpha} B^*_{\parallel\alpha} f_\alpha\right) = 0. \tag{1}$$

In Eq. (1), the differential operator $\nabla_{\mathbf{R}}$ performs differentiation with respect to the guiding center coordinates (the subscript $_{\mathbf{R}}$ will be omitted later in the paper for simplicity), $B^*_{\parallel\alpha}$ is the projection of $\mathbf{B}^*_\alpha$ to the magnetic field direction $\mathbf{b} = \mathbf{B}/B$, and $\mathbf{B}^*_\alpha$ is given by

$$\mathbf{B}^*_\alpha = \mathbf{B} + \frac{m_\alpha c v_\parallel}{q_\alpha} \nabla \times \mathbf{b}. \tag{2}$$

In the gyrokinetic approach, particles move along the magnetic field $\mathbf{B}$ with parallel velocity $v_\parallel$ and parallel acceleration

$$\dot{v}_{\parallel\alpha} = -\frac{\mathbf{B}^*_\alpha \cdot \mathbf{G}_\alpha}{m_\alpha B^*_{\parallel\alpha}}, \tag{3}$$

and exhibit perpendicular drifts with a guiding-center velocity $\dot{\mathbf{R}}_\alpha$ given by

$$\dot{\mathbf{R}}_\alpha = \frac{v_\parallel}{B^*_{\parallel\alpha}} \mathbf{B}^*_\alpha + c \frac{\mathbf{b} \times \mathbf{G}_\alpha}{q_\alpha B^*_{\parallel\alpha}}. \tag{4}$$

Here, $\mathbf{G}_\alpha$ is defined by

$$\mathbf{G}_\alpha = q_\alpha \nabla\phi + \mu_\alpha \nabla B, \tag{5}$$

where $\mu_\alpha = \frac{m_\alpha v_\perp^2}{2B}$ is the particle magnetic moment, m_α and q_α are the particle mass and charge, c is the speed of light, and ϕ is the electrostatic potential. In electrostatic gyrokinetics, Eq. (1) is coupled with the gyrokinetic Poisson equation[30] (GPE), which in the limit of small Larmor radius reads as

$$q(n_i - n_e) = -\frac{\nabla^2\phi}{4\pi} + \sum_\alpha \nabla_\perp \cdot \left(\frac{q_\alpha^2 n_\alpha}{m_\alpha \omega_{c\alpha}^2} \nabla_\perp \phi\right). \tag{6}$$

$\omega_{c\alpha} = \frac{q_\alpha B}{m_\alpha c}$ is the particle gyrofrequency and $n_{i,e}$ are gyrodensities of electrons and ions. The last term on the RHS (right-hand side) of Eq. (6) scales with $\omega_{pi}^2/\omega_{ci}^2$, where $\omega_{pi}^2 = 4\pi n_i q_i^2/m_i$ is the square of the ion plasma frequency. Thus, for perpendicular dynamics, this term is larger than the first term on the RHS for $\omega_{pi}^2 \gg \omega_{ci}^2$. Considering this limit, the GPE for the problem of interest in this work reduced to

$$q(n_i - n_e) = \frac{1}{r}\frac{\partial}{\partial r}\left(\frac{r m_i n_i c^2}{B^2}\frac{\partial\phi}{\partial r}\right) + \frac{\partial}{\partial z}\left(\frac{m_i n_i c^2}{B^2}\frac{\partial\phi}{\partial z}\right). \tag{7}$$

The gyrokinetic formalism is valid in strongly magnetized plasmas, i.e., when spatial scales of equilibrium parameters, such as density,

temperature, and magnetic field, are much greater than the largest gyroradius of all species $\rho_\alpha = V_{t\alpha}/\omega_{c\alpha}$, where $V_{t\alpha} = \sqrt{T_\alpha/m_\alpha}$ is the thermal speed. The characteristic spatial scale is the pinch radius r_0 and the ion gyroradius is the largest. Thus, the gyrokinetic formalism is valid for $\epsilon_L = \rho_i/r_0 \ll 1$. The second requirement is that characteristic frequencies of the processes of interest should be much smaller than the smallest gyrofrequency, $\epsilon_\omega = \omega/\omega_{ci} \ll 1$. The characteristic frequencies of the problem are that associated with the Alfvén transit time across the pinch, $\omega \sim V_a/r_0$, and thus $\epsilon_L = \epsilon_\omega = \epsilon$.

The aim of the present work is to simulate perturbed mode behavior in a sheared flow Z-pinch. For a given axial velocity profile $v_{zi}(r)$ [and also pressure $P(r)$ and magnetic field $B(r)$ profiles], force balance for each species can be used to find the corresponding electrostatic field $\mathbf{E}$ that is consistent with the desired velocity profile

$$\frac{\mathbf{v}_{i,e}}{c} = \frac{\mathbf{E}\times\mathbf{B}}{B^2} \mp \frac{\nabla P_{i,e}\times\mathbf{B}}{qnB^2}. \tag{8}$$

Notice that the difference of Eqs. (8) written for electrons and ions yields to the traditional MHD force balance equation $\nabla P = \mathbf{j}\times\mathbf{B}/c$. The electrostatic field $\mathbf{E}$ can be found from Eq. (8) using provided functions $v_{zi}(r)$, $P_i(r) = P_e(r)$, and $B(r)$, which can then be used to determine v_{ze}. In order to initialize the code with the self consistent equilibrium field $\mathbf{E}$, the gyrokinetic Poisson equation (7) is used, where the gyrodensity difference consistent with the equilibrium electric field is found as

$$\frac{\delta n}{n_i} = \frac{n_i - n_e}{n_i} \sim \frac{m_i c^2 E}{qrB^2}. \tag{9}$$

The last term in Eq. (8) is of the order

$$\frac{\nabla P\times\mathbf{B}}{qnB^2} \sim \frac{T}{rqB} \sim \frac{mc}{qB}\frac{V_t^2}{cr} \sim \frac{\rho_i}{r}\frac{V_t}{c} \sim \epsilon\frac{V_t}{c}. \tag{10}$$

If all the terms in Eq. (8) are of the same order, then the drift velocity can be estimated as $v_d \sim \epsilon V_t$, and E/B in Eq. (9) is of order $\epsilon V_t/c$, thus $\delta n/n_i \sim \epsilon^2$. However, for academic purposes and to be in a match with kinetic simulation results,[29] higher values of drift equilibrium velocity, up to $v_d \sim V_t$, can also be considered. In this case, E/B scales like V_t/c and $\delta n/n_i \sim \epsilon$. The gyrokinetic approach is not strictly valid for such high drift velocities, as Eq. (5) is missing high order terms that become comparable to the retained magnetic term in Eq. (5), and therefore possibly change the drift motion. Yet, shear velocities observed in experiments[10] are considerably slower than V_t, and most of our simulations are done for subsonic flows as well.

The set of equations (1)–(6) supports multiple solutions for the equilibrium, even unphysical ones, if all equilibrium quantities depend on the radial coordinate only. Indeed, $\mathbf{G}_\alpha$ has radial components only in this case, while both $\mathbf{B}^*$ and $\dot{\mathbf{R}}$ do not have this component. As a result, the second and the third terms in Eq. (1) are exactly zero, so any possible radial-dependent gyrokinetic distribution function is a solution. For the analysis in this work, the commonly used Bennett equilibrium profile is considered,[4,31–33] which provides the ion density and the magnetic field as follows:

$$n = \frac{n_0}{(1+\xi^2)^2}, \tag{11}$$

$$\mathbf{B} = \hat{\theta}\frac{2B_0\xi}{(1+\xi^2)}, \tag{12}$$

where $\xi = r/r_0$, n_0 and B_0 are density and magnetic field amplitudes, r_0 is the radial characteristic size of the pinch. Bennett equilibrium is derived under the following set of assumptions: (i) All quantities depend on the radial coordinate only; the pinch is infinitely long in the axial direction. (ii) Both species are streaming in the axial direction with velocities v_i and v_e, which are constant in space and time; electron-ion collisions do not change these velocities. (iii) Both species have Maxwellian distribution function with temperatures T_i and T_e, respectively, and these temperatures are constant in space and time. The difference between the ion and electron densities is relativistically small, i.e., of the order $\max(v_i^2, v_e^2)n_i/c^2 \sim \epsilon^2 n_i\omega_{ci}^2/\omega_{pi}^2$, yet sufficient enough to create charge separation and the corresponding electrostatic force comparable with the magnetic component of the Lorentz force. Notice, however, that this density difference is different from the one obtained in Eq. (9) for the gyrocenter densities, and therefore smaller by a factor $\omega_{ci}^2/\omega_{pi}^2$. The simulations are performed considering a frame where the electrostatic field in the shear-free case vanishes, namely, when $v_i = -v_e = v_0$. Furthermore, assuming that electrons and ions have the same temperature T_0, and considering singly ionized ions, $q_i = -q_e = q$, we obtain the following useful relations between various pinch parameters: Relation between the magnetic field amplitude and the streaming velocity

$$\frac{v_0}{c} = \frac{B_0}{2\pi q n_0 r_0}, \tag{13}$$

which can be obtained from Eq. (8); expression for the temperature in terms of the density and magnetic field amplitude

$$T_0 = \frac{B_0^2}{4\pi n_0}, \tag{14}$$

expression for the linear particle density N_L

$$N_L = \pi r_0^2 n_0, \tag{15}$$

and for the total current I

$$I^2 = 4c^2 N_L T_0 = c^2 B_0^2 r_0^2. \tag{16}$$

Also, notice that the characteristic Alfvén velocity defined using the peak density and the peak magnetic field is the same as the ion thermal speed

$$V_a^2 = \frac{B_0^2}{4\pi m_i n_0} = \frac{T_0}{m_i} = V_{ti}^2. \tag{17}$$

Equations (13)–(17) provide a set of constraints for Bennett equilibria. The values used in our simulations for the pinch radius r_0, peak density n_0, and magnetic field B_0 are taken from experimental data. Sheared flows are studied using a linear shear profile; therefore, ion and electron velocities read as

$$v_{i,e} = \pm v_0 + v_s, \tag{18}$$

where shear velocity is defined as

$$v_s = \kappa\xi V_a. \tag{19}$$

Here, κ is a dimensionless coefficient that determines shear strength, later in the paper called "shear parameter." Such shear does not change the total current and produced magnetic field; thus the equilibrium profile for density remains the same.

The simulations are performed using parameters characteristic of the FuZE[23] experiment, namely, $r_0 = 0.091$ cm, $n_0 = 4.25 \times 10^{18}$ cm^{-3}, $B_0 = 32$ T, $T_0 = 1198$ eV [obtained from Eq. (14) to be consistent with the Bennett profile]. At peak magnetic field, the gyroradius of the ion is small $\rho_i/r_0 \approx 0.12$. The domain in the radial direction spans from $r_{\min}$ to $r_{\max}$, where $r_{\min}$ varies from 0.05 to 0.07 cm and $r_{\max}$ from 0.15 to 0.30 cm, depending on the mode wave length and on the shear strength. The largest value of ϵ is reached at $r = 0.30$ cm: $\epsilon \approx 0.21$, yet the modes considered in this work are localized at smaller r, so the errors on the boundary are not important. The zero Dirichlet boundary condition (BC) is used for the electrostatic potential at $r = r_{\max}$, assuming a conducting wall at the outer boundary, and Neumann boundary condition at $r = r_{\min}$, where the potential derivative is in agreement with Eq. (8) to produce the right value of shear velocity. Note that the zero Dirichlet BC for the potential enforces zero particle flux at the outer radial boundary, and therefore a boundary condition for the distribution function is not required. At the inner radial boundary, the inflow boundary condition corresponds to a Maxwellian distribution function with $n_0(r_{\min})$ and T_0. Such boundary conditions can be adequate for the case where the mode structure is localized to the domain interior and does not extend to the inner radial boundary. Moreover, boundary conditions for the electrostatic potential can change the structure of the mode and hence have an impact on the growth rate if the radial size of the domain is small or even comparable to the physical radial scale of the mode. This is the reason why different domain sizes are used in the $\hat{r}$-direction depending on the mode number k_z—the radial extent of the mode is smaller for higher k_z. In each of the simulations, the outer radial boundary is chosen to be large enough such that it has no effect on the radial size of the mode. The noticeable variation of the growth rate, associated with an improper radial boundary size, is approximately 10%.

In the axial direction, the domain resolves only one full wave length of the seeded mode ($z_{\min} = 0$, $z_{\max} = \lambda$) and periodic boundary conditions are used.

The mode was seeded by initial density perturbation

$$n_i(r,z) = n_{i0}(r) \cdot (1 + \cos(k_z z) g(r)), \tag{20a}$$

$$n_e(r,z) = n_{i0}(r) \cdot (1 - \cos(k_z z) g(r)) - \delta n(r), \tag{20b}$$

where $k_z = 2\pi/z_{\max}$, δn is the equilibrium density difference from Eq. (7) that supports sheared flow, and $g(r, \bar{r}_c, a_0)$ is the radial envelope with amplitude A, center $\bar{r}_c$, and width a_0

$$g(r, \bar{r}_c, a_0) = A \exp\left(-\frac{(r - \bar{r}_c)^2}{a_0^2}\right). \tag{21}$$

Parameters A, $\bar{r}_c$, and a_0 are chosen individually for every value of k_z in order be in close radial match to the eigenmode. The amplitude is chosen to be small enough to observe the linear growth rate of the mode for the longest possible time, yet large enough to seed the mode and distinguish it from the numerical noise. The values used here range from 10^{-7} to 10^{-4}. Center $\bar{r}_c$ and width a_0 are usually picked after a preliminary run of a coarse resolution and are $r_c \sim 1.1 - 1.8 r_0$, and $a_0 \sim 0.1 - 0.5 r_0$. No seeded temperature perturbation is used in all the runs.

Spatial grid resolution is varied depending on the mode wave number k_z. Due to high order spatial discretization of the code, even a relatively coarse resolution, e.g., 32×32, in the $R \times Z$ plane is sufficient to provide an accurate mode structure and growth rates for all modes in the shear-free case (see Sec. V for more details). In the case of a strong shear flow, the resolution is increased up to 128×64 in order to resolve a fine mode structure adequately. The code employs an explicit time advance scheme Runge-Kutta(4,4); therefore the time step is limited by the Courant Friedrichs Lewy (CFL) constraint, and decreases as the resolution or the mode wave number increases.

III. LINEAR DISPERSION ANALYSIS

A linear dispersion relation obtained from the governing equations in a simplified case is presented and examined in this section. This provides some insight into the what types of modes are expected in the simulations.

Refer to gyrokinetic equations (1)–(6). Consider electrostatic problem with given magnetic field of the shape $\mathbf{B} = \hat{\theta} B(r)$, then $(\nabla \times \mathbf{b})_\perp = \hat{z}/r$ and $\nabla B = \hat{r}\frac{\partial B}{\partial r}$. Under the assumptions of axial symmetry, i.e., $\partial/\partial\theta = 0$ we have the following expressions for drift velocity and acceleration:

$$\dot{\mathbf{R}}_\alpha = v_\parallel \hat{\theta} + c\frac{m_\alpha v_\parallel^2}{q_\alpha r B}\hat{z} + \frac{c}{q_\alpha B}\left(\hat{r} q_\alpha \frac{\partial \phi}{\partial z} - \hat{z} q_\alpha \frac{\partial \phi}{\partial r} - \hat{z}\mu_\alpha \frac{\partial B}{\partial r}\right), \tag{22a}$$

$$\dot{v}_\parallel = -\frac{c v_\parallel}{rB}\frac{\partial \phi}{\partial z}. \tag{22b}$$

Substitute Eq. (22) into Eq. (1) to obtain

$$\frac{\partial f_\alpha}{\partial t} + \left(\frac{m_\alpha c v_\parallel^2}{q_\alpha r B} - \frac{c}{B}\frac{\partial \phi}{\partial r} - \frac{c\mu_\alpha}{q_\alpha B}\frac{\partial B}{\partial r}\right)\frac{\partial f_\alpha}{\partial z} + \frac{c}{B}\frac{\partial \phi}{\partial z}\frac{\partial f_\alpha}{\partial r} - \frac{c v_\parallel}{Br}\frac{\partial \phi}{\partial z}\frac{\partial f_\alpha}{\partial v_\parallel} = 0. \tag{23}$$

By choosing a frame where the equilibrium electric field is identically zero, the term $\partial\phi/\partial r$ vanishes in the shear-free case (see Sec. II). When the shear is present, the equilibrium electric field remains due to charge separation in the GPE that establishes shear flow.

Make use of $\mu_\alpha = m_\alpha v_\perp^2/(2B)$ to get

$$\frac{\partial f_\alpha}{\partial t} + \frac{c}{B}\frac{\partial \phi}{\partial z}\frac{\partial f_\alpha}{\partial r} + \frac{m_\alpha c}{q_\alpha r B}\left(v_\parallel^2 + \frac{v_\perp^2}{2}\psi\right)\frac{\partial f_\alpha}{\partial z} - \frac{c}{B}\frac{\partial \phi}{\partial r}\frac{\partial f_\alpha}{\partial z} - \frac{c v_\parallel}{rB}\frac{\partial \phi}{\partial z}\frac{\partial f_\alpha}{\partial v_\parallel} = 0, \tag{24}$$

where $\psi = -\frac{r}{B}\frac{\partial B}{\partial r}$. For Bennett profile magnetic field Eq. (12), we have $\psi = (\xi^2 - 1)/(\xi^2 + 1)$, which goes to the toroidal field limit as $\xi \to \infty$ and to the constant field limit as $\xi = 1$.

Consider the equilibrium distribution function

$$f_{0\alpha} = \left(\frac{m_\alpha}{2\pi T_\alpha}\right)^{3/2} n_{0\alpha}(r) \exp\left(-\frac{m_\alpha v_\parallel^2}{2T_\alpha} - \frac{\mu_\alpha B}{T_\alpha}\right), \tag{25}$$

and a small perturbation of the distribution function $\tilde{f}_\alpha \exp(-i\omega t + ik_z z)$ with a corresponding electrostatic potential $\tilde{\phi}\exp(-i\omega t + ik_z z)$. In a linear order, the kinetic equation for perturbations reads as

$$-i\omega\tilde{f}_\alpha + ik_z\frac{m_\alpha c}{q_\alpha rB}\tilde{f}_\alpha\left(v_\parallel^2+\frac{v_\perp^2}{2}\psi\right) - ik_z\frac{c}{B}\tilde{f}_\alpha\frac{\partial\phi_0}{\partial r} + ik_z\tilde{\phi}\left(\frac{c}{B}\frac{\partial f_{0\alpha}}{\partial r} - \frac{cv_\parallel}{rB}\frac{\partial f_{0\alpha}}{\partial v_\parallel}\right) = 0. \tag{26}$$

The radial derivative of the potential can be replaced by the electric field $E = -\frac{\partial\phi_0}{\partial r}$. Use Eq. (25) to find derivatives for Eq. (26)

$$\frac{\partial f_{0\alpha}}{\partial r} = \frac{\partial n_{0\alpha}}{\partial r}\frac{f_{0\alpha}}{n_{0\alpha}} - \frac{f_{0\alpha}\mu_\alpha}{T_\alpha}\frac{\partial B}{\partial r} = -\frac{f_{0\alpha}}{L_\alpha} + \frac{f_{0\alpha}\psi}{r}\frac{m_\alpha v_\perp^2}{2T_\alpha}, \tag{27a}$$

$$\frac{\partial f_{0\alpha}}{\partial v_\parallel} = -f_{0\alpha}\frac{m_\alpha v_\parallel}{T_\alpha}, \tag{27b}$$

where $n_0 L_\alpha^{-1} = -\frac{\partial n_{0\alpha}}{\partial r}$, and express the distribution function in terms of the perturbed potential

$$\tilde{f}_\alpha = \tilde{\phi}\frac{k_z c f_{0\alpha}}{B}\cdot\frac{\frac{1}{L_\alpha} - \frac{m_\alpha}{rT_\alpha}\left(v_\parallel^2+\frac{v_\perp^2}{2}\psi\right)}{-\omega + \frac{k_z m_\alpha c}{q_\alpha rB}\left(v_\parallel^2+\frac{v_\perp^2}{2}\psi\right) + \frac{ck_zE}{B}}. \tag{28}$$

All parameters in Eq. (28) are functions of the radial coordinate. To make an analytical progress, we assume $kr_0 \gg 1$ and fix the values of the background profiles at some given value of r. The density perturbation then reads as

$$\tilde{n}_\alpha = \int_{-\infty}^{\infty} dv_\parallel \int_0^{\infty} 2\pi v_\perp dv_\perp \tilde{f}_\alpha. \tag{29}$$

The velocity-dependent part can be removed from the numerator of Eq. (28), so that Eq. (29) takes the following form:

$$\begin{aligned}\tilde{n}_\alpha &= -\frac{q_\alpha n_{0\alpha}\tilde{\phi}}{T_\alpha} + \frac{q_\alpha n_{0\alpha}\tilde{\phi}}{T_\alpha}\left(\frac{m_\alpha}{2\pi T_\alpha}\right)^{3/2} \\ &\times \int_{-\infty}^{\infty} dv_\parallel \int_0^{\infty} \pi d(v_\perp^2)\exp\left[-\frac{m_\alpha v_\parallel^2}{2T_\alpha} - \frac{m_\alpha v_\perp^2}{2T_\alpha}\right] \\ &\times \frac{\frac{\omega q_\alpha rB}{km_\alpha c} - \frac{q_\alpha rE}{m_\alpha} - \frac{rT_\alpha}{m_\alpha L_\alpha}}{\frac{\omega q_\alpha rB}{km_\alpha c} - \frac{q_\alpha rE}{m_\alpha} - \left(v_\parallel^2+\frac{v_\perp^2}{2}\psi\right)} \\ &= -\frac{q_\alpha n_{0\alpha}\tilde{\phi}}{T_\alpha} + \frac{q_\alpha n_{0\alpha}\tilde{\phi}}{\sqrt{\pi}T_\alpha}\int_{-\infty}^{\infty} dy \int_0^{\infty} 2xdx\exp\left(-x^2-y^2\right) \\ &\times \frac{W - \frac{r}{2L_\alpha}}{W - \left(y^2+\frac{\psi}{2}x^2\right)}.\end{aligned} \tag{30}$$

In Eq. (30), $W = [\omega - \frac{ck_zE}{B}]\cdot\frac{rq_\alpha B}{2ck_zT_\alpha}$, which will be of different sign for electrons and ions.

The integral Eq. (30) is similar to one in Ricci's work[18] but here we miss the term $1 - k^2v_\perp^2/2\omega_{ci}^2$. This is a pressure correction term[30] that is small in the long-wavelength limit and is neglected in the present "minimal" model. The integral in Eq. (30) can be taken analytically only in some special cases: $\psi = 1$ and $\psi = 0$. For $\psi = 1$

$$\begin{aligned}I_1 &= -e^{-2w}\int_0^{\infty} 2xdx\frac{e^{w-x^2/2}}{\sqrt{x^2/2-w}}\operatorname{erfc}\left(\sqrt{x^2/2-w}\right) \\ &= -e^{-2w}\pi^{3/2}\operatorname{erfc}^2\left(\sqrt{-w}\right),\end{aligned} \tag{31}$$

and for $\psi = 0$

$$\begin{aligned}I_0 &= -e^{-2w}\int_0^{\infty} 2xdx\frac{e^w}{\sqrt{-w}}\operatorname{erfc}\left(\sqrt{-w}\right) \\ &= \frac{e^{-w}\pi w}{(-w)^{3/2}}\operatorname{erfc}\left(\sqrt{-w}\right).\end{aligned} \tag{32}$$

Assume equal temperatures $T_i = T_e = T$, and then $W = W_i = -W_e$. Expressions for the ion and electron densities for arbitrary ψ read as

$$\tilde{n}_i = -\frac{qn_{0i}\tilde{\phi}}{T} + \frac{qn_{0i}\tilde{\phi}}{\sqrt{\pi}T}\left(W - \frac{r}{2L_i}\right)I_\psi(W), \tag{33a}$$

$$\tilde{n}_e = +\frac{qn_{0e}\tilde{\phi}}{T} - \frac{qn_{0e}\tilde{\phi}}{\sqrt{\pi}T}\left(-W - \frac{r}{2L_e}\right)I_\psi(-W), \tag{33b}$$

where I_ψ is chosen according to the value of r.

W or ω can be found by substitution of Eq. (33) into the gyrokinetic Poisson equation (7). In the limit of short-scale perturbations, the GPE can be modified as follows:

$$\begin{aligned}\nabla_\perp\cdot\left(\frac{m_i(n_{i0}+\tilde{n}_i)c^2}{B^2}\nabla_\perp\phi\right) &= \frac{m_ic^2}{B^2r}\frac{\partial}{\partial r}\left(rn_{i0}\frac{\partial\phi_0}{\partial r}\right) + \frac{m_ic^2}{B^2r}\frac{\partial}{\partial r} \\ &\times\left(rn_{i0}\frac{\partial\tilde{\phi}}{\partial r}\right) + \frac{m_ic^2}{B^2r}\frac{\partial}{\partial r}\left(r\tilde{n}_i\frac{\partial\phi_0}{\partial r}\right) \\ &+ \frac{m_in_{i0}c^2}{B^2}\frac{\partial^2\tilde{\phi}}{\partial z^2}.\end{aligned} \tag{34}$$

The first term on the right hand side of Eq. (34) is the equilibrium shear flow term, which is not a perturbation, and therefore exactly cancels the other equilibrium terms in the GPE. Higher order term $O(\tilde{n}_i\tilde{\phi})$ is omitted as we are doing linear analysis. In the remaining two terms, the differential operator applies to $\tilde{\phi}$ and $\tilde{n}_i$ only, assuming that background quantities have a large spatial scale compared to the perturbation scale. Finally, the radial structure of the mode can be considered as a half sinusoidal if the boundary conditions are such that $\tilde{\phi} = 0$ on the radial boundaries. In this case, the wave number can be expressed as $k_r = \pi/L_r$, where L_r is the radial domain length and the following replacements $\partial/\partial r = ik_r$, $\partial/\partial z = ik_z$ can be made. Taking into account all these assumptions, we obtain the GPE for the perturbed quantities

$$\begin{aligned}q(\tilde{n}_i - \tilde{n}_e) &= -\nabla_\perp\cdot\left(\frac{m_in_ic^2}{B^2}\nabla_\perp\phi\right) \\ &= \frac{m_in_{i0}c^2}{B^2}(k_r^2+k_z^2)\tilde{\phi} + i\frac{m_ik_rc^2E}{B^2}\tilde{n}_i,\end{aligned} \tag{35}$$

where $\tilde{n}_i$ and $\tilde{n}_e$ are from Eqs. (33).

Consider a simple case of long-wavelength perturbations in a shear-free flow pinch. Electrostatic field is zero; therefore, $W = \frac{\omega rqB}{2ck_zT}$. The ideal MHD interchange mode[7] has a growth rate of the order

$\mathrm{Im}[\omega] = \gamma \sim V_t/r_0$. Therefore, $W \sim \frac{V_t q B m}{2cmk_z T} = \frac{1}{k_z \rho_i} \gg 1$, and the integral in Eq. (30) can be approximated by Taylor expanding the denominator

$$I_\psi(w) \approx \int_{-\infty}^{\infty} dy \int_0^{\infty} 2x dx \exp\left(-x^2 - y^2\right) \times \left(\frac{1}{w} + \frac{y^2}{w^2} + \frac{\psi x^2}{2w^2} + \frac{(2y^2 + \psi x^2)^2}{4w^3}\right) = \frac{\sqrt{\pi}}{w}\left(1 + \frac{1}{2w} + \frac{\psi}{2w} + \frac{3}{4w^2} + \frac{\psi^2}{2w^2} + \frac{\psi}{2w^2}\right). \quad (36)$$

Substitute this expression into Eq. (35)

$$\frac{q^2}{T}\left[-2 + \left(1 - \frac{r}{2WL_n}\right) I_\psi(W) + \left(1 + \frac{r}{2WL_n}\right) I_\psi(-W)\right] = \frac{m_i c^2 (k_r^2 + k_z^2)}{B^2}, \quad (37)$$

and solve for ω

$$\omega^2 = \frac{2T}{m_i r^2} \cdot \frac{k_z^2}{k_z^2 + k_r^2}\left[3 + (\psi + 1)\left(2\psi - \frac{r}{L_n}\right)\right]. \quad (38)$$

As it follows from Eq. (38), ω can be either real or imaginary, meaning exponential growth for the latter. For $\psi = 1$, the ideal mode stability condition is $L_n/r > 2/7$, in agreement with the result from Ricci's paper[18] in the collisionless limit. The magnitude of ω is the same as initially assumed $\omega \sim V_t/r_0$, so the result in Eq. (38) is valid as long as the expression in square parentheses is not close to zero.

For the Bennett profile, ψ and L_n can be expressed as functions of ξ

$$\psi = \frac{\xi^2 - 1}{\xi^2 + 1}; \quad \frac{r}{L_n} = \frac{4\xi^2}{\xi^2 + 1}. \quad (39)$$

To find the stability condition, evaluate the square parentheses with substitutions from Eq. (39)

$$\left[3 + (\psi + 1)\left(2\psi - \frac{r}{L_n}\right)\right] = \frac{3 - \xi^2}{1 + \xi^2}. \quad (40)$$

The expression in Eq. (40) is positive for $\xi < \sqrt{3}$, so the ideal MHD mode is stable for $\xi \approx 1$. This is in agreement with the simulations results, where the center of the mode is localized at $\xi \geq \sqrt{3}$ for low k_z modes. Notice though that the $m = 0$ mode is always unstable for the Bennett profile[27] in the ideal MHD analysis, if $\bar{\gamma} < 2$, where $\bar{\gamma}$ is the heat capacity ratio $\bar{\gamma} = c_p/c_v$. This contradictory result can be explained by the fact that our model is kinetic, therefore does not contain an adiabatic closure for pressure terms, and is also collisionless.

In order to investigate the dispersion relation in the general case, Eq. (35) needs to be analyzed on a complex plane and the roots have to be determined numerically. For simplicity, one can assume a large scale radial structure of the modes $k_r = 0$, yet still small compared to the pinch radius. The normalized growth rate for both $\psi = 0$ and $\psi = 1$ is shown in Fig. 1.

There are some important observations that can be made here. First, the shear effect does not change the growth rate much. The main contribution of the shear is through the electric field, which changes W

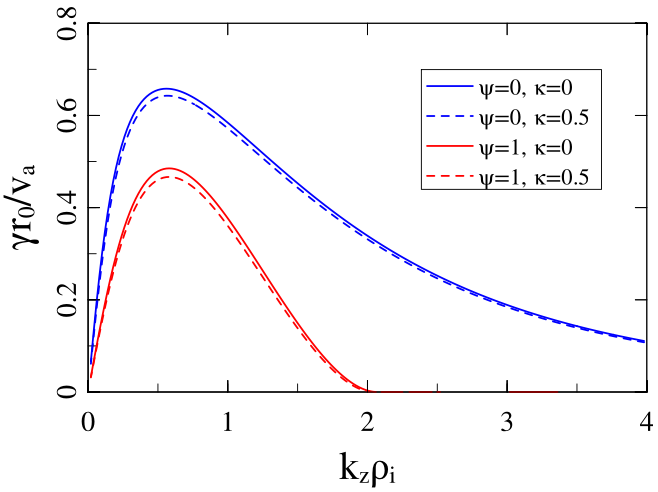

FIG. 1. Normalized growth rate of a local entropy mode at $r = r_0$ as a function of wave number k_z at $k_r = 0$ for constant ($\psi = 0$) and toroidal ($\psi = 1$) magnetic fields and for two values of the shear parameter. Solid line: No shear $\kappa = 0.0$; dashed line $\kappa = 0.5$.

$$W = \left[\omega - \frac{ck_z E}{B}\right] \cdot \frac{rq_\alpha B}{2ck_z T_\alpha}. \quad (41)$$

It adds the real part to ω, making the perturbation drift with $\mathbf{E} \times \mathbf{B}$ velocity. The second contribution of the shear is the change of background electron density in Eq. (35). These changes are however small as parameter ϵ is small that is always assumed.

Second, the growth rate for $\psi = 1$ case has a cutoff at $k_z \rho_i \approx 2$. In fact, the condition should be $(k_z^2 + k_r^2)\rho_i^2 \approx 4$, since k_z and k_r appear exactly in such a combination in Eq. (35). In a realistic scenario, ψ is expected to be between 0 and 1, therefore the cutoff to be at some higher values of $k\rho_i$, yielding to FLR stabilization of the mode. The polarization terms in the GPE are indeed important: A simplified version of the gyrokinetic Poisson equation ($n_i - n_e = 0$) provides the linear dependence of the growth rate on k_z but does not have any cutoff or even decay at high values of k_z.

The current linear analysis helps to describe the mode behavior only qualitatively. First, the derived result is valid for local modes, while the modes of interest have a radial size of the order of r_0 and are thus global. Second, the exact analytical dispersion relation is not known for an arbitrary value of ψ in the interval [0,1] and the behavior can only be anticipated to be similar to the cases of $\psi = 0$ and $\psi = 1$. Finally, and most important, some of the FLR terms are not correctly taken into account, like no gyroaveraging for particle drifts, the long-wavelength limit for the gyrokinetic Poisson equation, or missing pressure terms[18] in density integrals. However, even inclusion of the polarization term in the long-wavelength limit in the GPE is enough to provide decreasing nature of the growth rate for high k, while the other effects change the cutoff value without changing the general picture dramatically.

IV. SIMULATION RESULTS

The main goal of the simulations is to find how the growth rate of the mode depends on the wave number k_z and shear parameter κ. Among all quantities, the axial component of the electric field is the

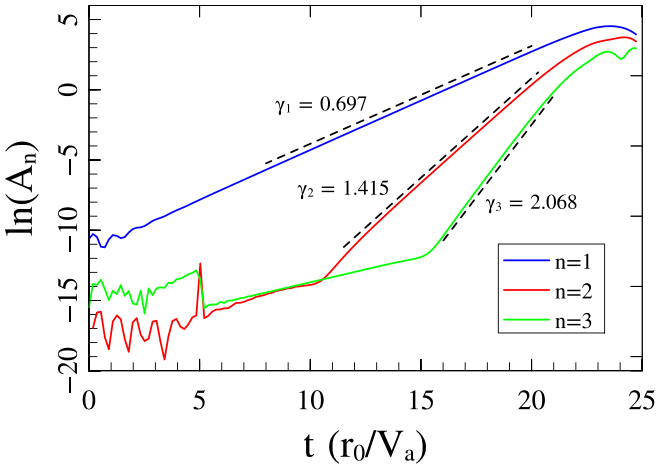

FIG. 2. Time evolution of the three harmonics A_1, A_2, and A_3 of the seeded mode with $k_z r_0 = 5$ and $\kappa = 0$. The growth rate at a linear stage is in units of inversed Alfvén time V_a/r_0.

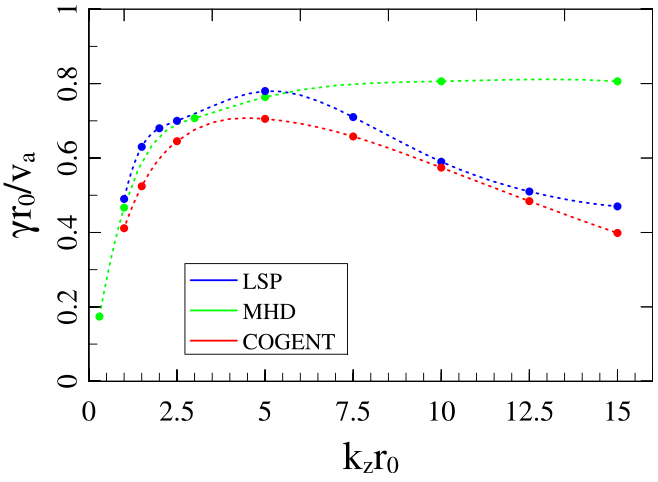

FIG. 3. Normalized growth γ of the seeded mode as a function of k_z for no shear flow $\kappa = 0$. Also comparison to the ideal MHD[27] and kinetic simulations (LSP).[29]

most informative and vivid one to provide the growth rate and the structure of the mode. Unlike the density or the potential in the sheared flow case, E_z has no mean part as $E_z = 0$ in the equilibrium, which makes it much better for illustration purposes. We also compare our results of the growth rate of the density perturbation and it is all consistent.

The growth rate is defined as follows. For a given value of k_z and κ, the "center" of the mode in the radial direction r_c is determined. At a given time t, the slice of the mode at $r = r_c$ provides a function of $E_z(z, t)$, which is Fourier decomposed to $n = 1, 2, 3$ modes (the seeded mode is $n = 1$). Fourier amplitude of the n-mode by our assumption grows as $A_n \propto \exp(\gamma_n t)$.

Such an approach in determining γ has advantages and disadvantages. It might suffer from the fact that r_c is not determined correctly, or the fact that the mode can slowly move in the radial direction as it evolves. It is especially noticeable at the beginning of the run when the eigenmode forms from the seeded perturbation. In order to mitigate these types of errors we wait for some time (usually, about 1–5 Alfvén times) and let the system settle. The alternative approach used in papers[27,29] is to consider a weighted radial integral of the mode instead of doing a fixed radius slice. This helps to avoid the mentioned problems but that does not well describe a growth rate of a very stretched "thin" mode, when the mode can wrap around the domain in the axial direction.

The time evolution of the first three harmonic amplitudes is demonstrated in Fig. 2. The main harmonic $n = 1$ starts from a value of 10^{-10} while the other two start from the numerical noise. Eventually they are settled by the time 10 and 15 Alfvén units and grow with double and triple growth rates, respectively. This is in agreement with

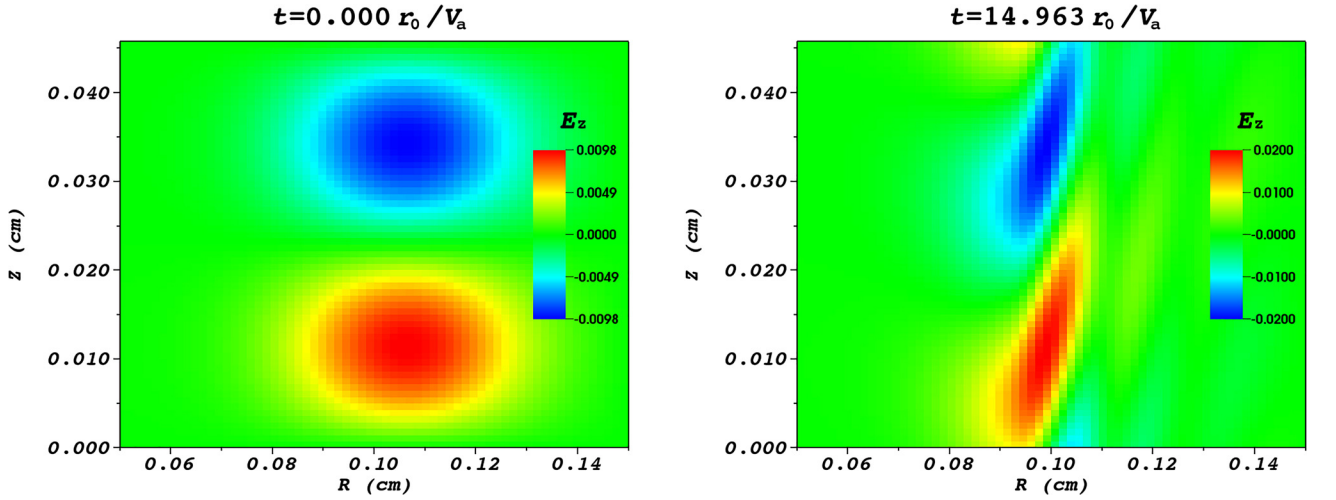

FIG. 4. Evolution of a mode with $k_z r_0 = 12.5$, and $\kappa = 0.25$. The initial seeded mode tilts and stretches along the axial direction, until it gets to the shape in the right picture, and then it slowly grows with the normalized growth rate $\gamma \approx 0.081\, V_a/r_0$ until it gets to the nonlinear stage.

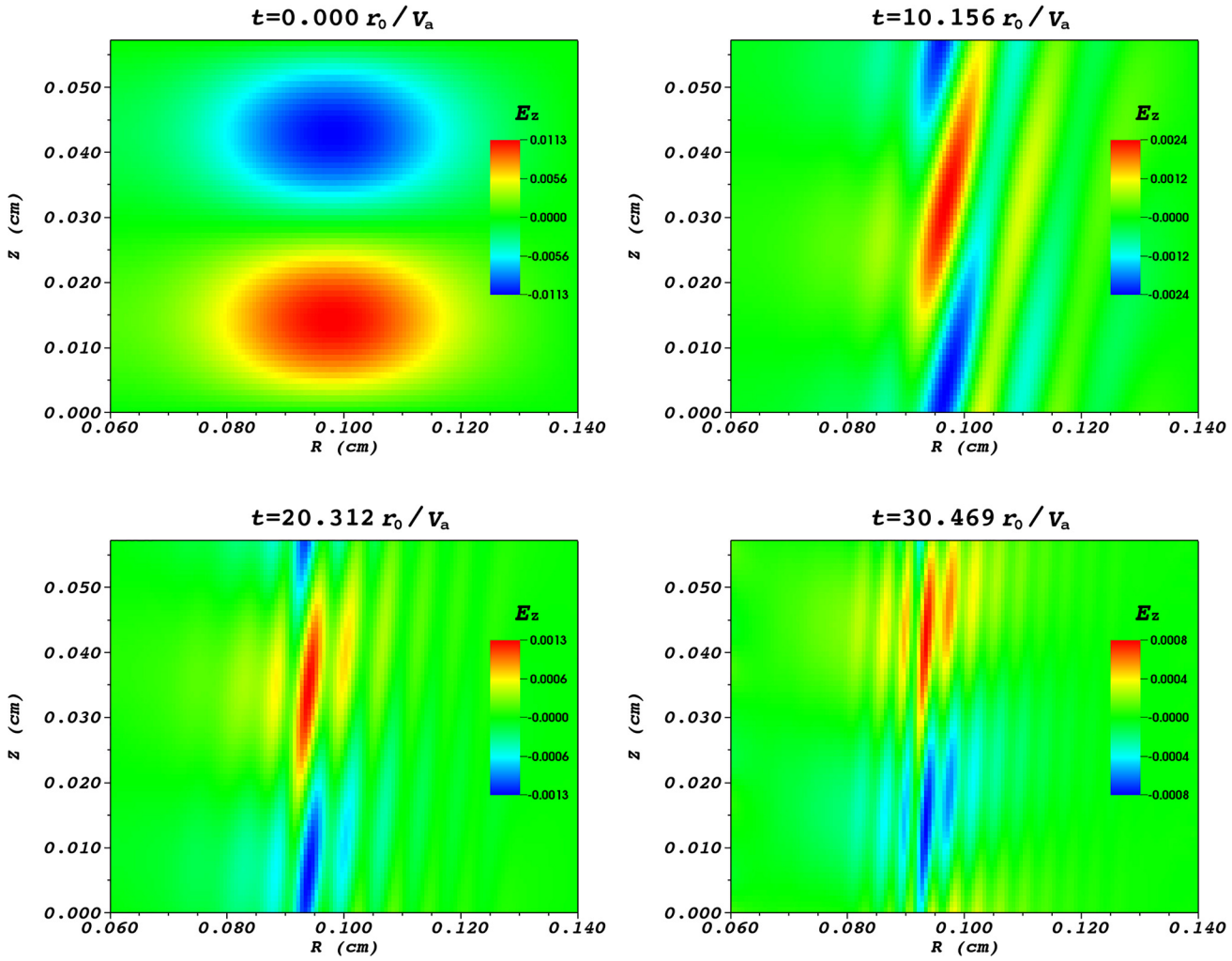

FIG. 5. Evolution of a seeded mode with $k_z r_0 = 10$, and $\kappa = 0.5$. The initial seeded mode tilts and stretches along the axial direction becoming very narrow in the radial direction. Such a structure slowly decays.

previous results from papers.[27,29] The weakly nonlinear mechanism of such growth rates of the higher harmonics is described by Book *et al.*[34]

The dependence of the growth rate on the mode number for shear-free flow is shown in Fig. 3. The behavior is qualitatively similar to the results of the growth rate obtained from the local linear dispersion relation Fig. 1. In particular, the growth rate scales linearly with k_z at small k_z, reaches its maximum value at $k_z r_0 \approx 5$, which corresponds to $k_z \rho_i \approx 0.6$, and slowly decays at higher k_z. These results are in good overall agreement with the results from fully kinetic PIC simulations.[29]

In the shear-free flow case, the mode structure is of the shape of two blobs of positive and negative perturbation. The structure is stationary, as the simulations are performed in a time frame where equilibrium electric field is zero. The radial size of the structure decreases as the wave number increases, so the mode does not change its structure much.

In the case of sheared flow, the mode drifts in the axial direction with $\mathbf{E} \times \mathbf{B}$ velocity, where the fields are determined by approximately the position of the center mass of the mode in the radial direction. Since the mode is initialized by the same type of perturbation as for the case of zero shear, the overlap between the eigen mode and the perturbation becomes small. Consequentially, the mode takes considerably more time to settle and get to the eigen state: It tilts and stretches due to the shear until it eventually gets to the shape shown in Fig. 4. The stretching is consistent with the shear parameter and gets stronger as κ increases. This circumstance makes the simulations less efficient, as a higher radial resolution is needed to resolve the structure correctly. Besides, the seeded perturbation now needs to be higher, because otherwise it will be washed away by a sheared flow and the mode will take dramatically longer time to grow from the numerical noise. Figure 5 shows how the seeded perturbation evolves in time in a sheared flow with $\kappa = 0.5$. It forms a structure which resembles an eigenmode but the amplitude slowly decays in time, demonstrating a shear stabilization effect. In high shear case $\kappa = 0.75$ most seeded modes are

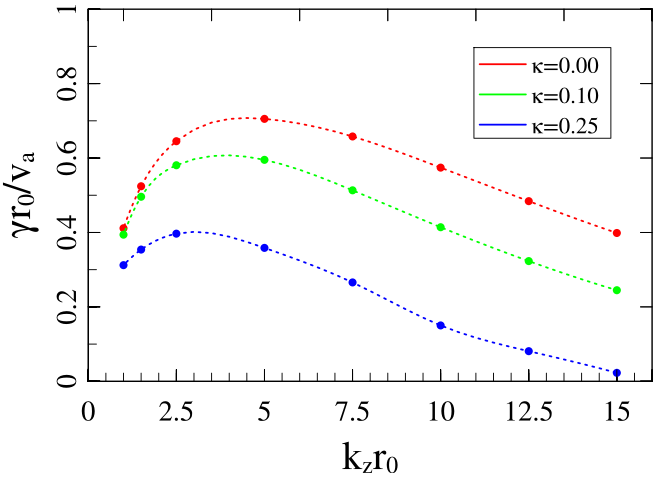

FIG. 6. Normalized growth rate γ of the seeded mode as a function of k_z for three values of the shear parameter κ. Red: $\kappa = 0$; green: $\kappa = 0.1$; blue: $\kappa = 0.25$.

immediately destroyed, as no instability is observed, though this result is on the limit of the applicability of our numerical model.

The growth rate is measured as a function of k_z for three different values of shear. The results are shown in Fig. 6. Slight shear, up to $\kappa = 0.25$, is unable to stabilize the mode; it, however, makes the growth rate smaller, which is especially noticeable for high-k_z modes.

To explain stabilization of the entropy mode by the sheared flow, refer to the local linear growth rate obtained from the dispersion relation shown in Fig. 1. Strongly sheared flow makes the mode stretched in the axial direction so much that its radial scale becomes very small; therefore k_r and total k become very large. As it was derived in Sec. III, the growth rate decreases for $\psi = 0$ and has a cutoff at high k for $\psi = 1$. In the simulations, the mode is localized at $r > r_0$, thus, somewhat intermediate behavior for the growth rate can be anticipated, or in other words, a cutoff at some large values k. This is what the shear flow effect on the mode is—it moves it to the cutoff region by increasing k_r, which yields to the stabilization mechanism.

V. DISCUSSION AND CONCLUSION

Electrostatic gyrokinetic simulations are demonstrated to be a very useful and appropriate tool for $m = 0$ modes in sheared flow Z-pinch plasmas. Inclusion of the second order FLR polarization term in the long-wavelength limit is shown to be sufficient to capture physics missing in MHD models and provide adequate dependence of the growth rate on the shear parameter κ and the mode wave number k_z, as demonstrated in Fig. 3. The high-order spatial discretization nature of the COGENT code allows speeding up the calculation dramatically. One can find comparison of a coarse run and a fine run in Fig. 7. The coarse run has a resolution $16 \times 16 \times 24 \times 24$ in the $R \times Z \times v_{\|} \times \mu$ configuration space, and the fine run has a resolution $64 \times 64 \times 48 \times 32$, which is 48 times greater in the total number of cells. The coarse resolution run provided the same mode structure as the fine resolution one. What is more important, the difference in growth rates is less than one percent, namely $\gamma_f = 0.698\, V_a/r_0$ for the fine run, and $\gamma_c = 0.693\, V_a/r_0$ for the coarse run. The speed up gain in terms of computer time is approximately by a factor of 70. A more detailed

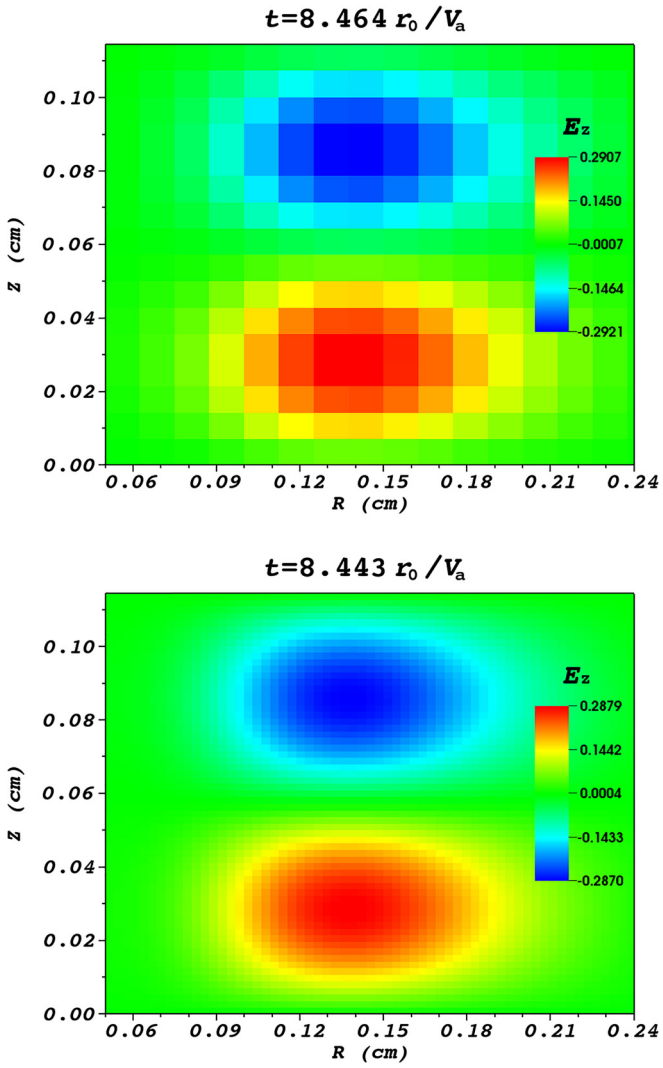

FIG. 7. Comparison of the mode structure for coarse and fine runs. Both pictures show the same mode at a linear growth stage at approximately the same time.

convergence study of the code, including difference of second and fourth order spatial discretization, is reported elsewhere.[35]

The benefits of using coarse resolution gyrokinetic simulations are even greater if compared to full kinetic or particle-in-cell simulations. For example, up to 500 times speed up was achieved when a coarse resolution was used for the same parameters of a shear-free mode as in recent PIC simulations.[29] In gyrokinetics, the fast electron gyroperiod time scale is not resolved; hence, the limitations are either due to the time scales of the simulated processes (in our case Alfvén time that is much greater than the electron gyroperiod) or due to numerical constraints, such as CFL conditions, which can cause a slow down of simulations for high-k modes and high shear parameter values. The CFL constraint can be in principle overcome by using implicit time integrators. Besides, compared to PIC simulations, gyrokinetic simulations do not suffer from statistical noise; therefore, a much clearer picture of a mode

structure can be obtained, including its evolution and distortion, like shown in Fig. 5.

The validity of the electrostatic approximation is worth discussing. Magnetic field changes and the electromagnetic part of the electric field are neglected in our model. A variation of the magnetic field δB can be estimated from the equality of the kinetic and magnetic pressures

$$\delta B B \sim 4\pi \delta P \sim 4\pi T \delta n_{\mathrm{T}}, \tag{42}$$

where δn_{T} denotes a small number density variation. In order to link it to the charge density variation δn in the GPE, think about the formation of the perturbation. Consider a parcel of excessive density at some radius r. Electrons and ions feel centrifugal and $\mu \nabla B$ forces in the radial direction and drift in the axial direction with $v_{i,e} \sim \pm c m_{i,e} v^2/(qrB)$. This drift motion creates charge separation $q\delta n$, which can be estimated from the continuity equation

$$\frac{\partial (q\delta n)}{\partial t} + \nabla \cdot \mathbf{j} = 0, \tag{43}$$

where $\mathbf{j}$ is the drift current and given by $q\hat{z}\delta n_{\mathrm{T}}(v_i - v_e)$, and its divergence has only one contribution in the $\hat{z}$ direction. Therefore, δn can be expressed in terms of δn_{T} as follows:

$$\delta n \approx \frac{k_z c T}{\omega q r B} \delta n_{\mathrm{T}}, \tag{44}$$

where ω is substituted instead $\partial/\partial t$, k_z instead of $\partial/\partial z$, and also small electron drift contribution is ignored. From Faraday's law, the ordering for curl $\mathbf{E}$ is obtained

$$|\nabla \times \mathbf{E}| \sim \frac{\omega}{c} \delta B \sim \frac{4\pi \omega T}{cB} \delta n_{\mathrm{T}}. \tag{45}$$

There are two main contributions of magnetic field variation to the system behavior. First, changing in time magnetic field creates nonpotential electric field (denote as $\mathbf{E}_{\sim}$). We can estimate this effect by comparing curl and divergence of the field $\epsilon_E = \frac{|\nabla \times \mathbf{E}_{\sim}|}{|\nabla_{\perp} \cdot \mathbf{E}_{\perp}|}$. Second, changed electric field and magnetic field alter particle drifts. For $\mathbf{E} \times \mathbf{B}$ drift, the effect is small, once ϵ_E is small; for ∇B drift, the effects will be evaluated separately.

Compare the electromagnetic part of electric field to the potential part $|\nabla_{\perp} \cdot \mathbf{E}_{\perp}|$. Make use of the GPE Eq. (6)

$$q\delta n \sim \frac{m_i n_i c^2}{B^2} \nabla_{\perp} \cdot \mathbf{E}_{\perp}, \tag{46}$$

together with Eq. (14) for temperature and find the ratio of electromagnetic to electrostatic parts

$$\epsilon_E = \frac{|\nabla \times \mathbf{E}_{\sim}|}{|\nabla_{\perp} \cdot \mathbf{E}_{\perp}|} \sim \frac{4\pi \omega^2 m_i n_i r}{B^2 k_z} = \frac{\omega^2 r}{V_t^2 k_z}. \tag{47}$$

The quantity in Eq. (47) should be much less than unity in order to neglect electromagnetic effects. For an ideal MHD mode, $\omega \sim V_t/r_0$, thus Eq. (47) reads as $\epsilon_E = (k_z r_0)^{-1} \ll 1$. In the simulations $k_z r_0$ is varied from 1.5 to 15, so electromagnetic effects might be important for small k_z ideal MHD modes. Notice, however, that in the long wavelength limit, the ideal MHD mode growth rate depends on k_z linearly; therefore, electromagnetic effect contribution remains bound and comparable to the electrostatic one. For the entropy mode, we anticipate to get different scaling for the growth rate[7] $\omega \sim k_z \rho_i V_t/r_0$; thus, Eq. (47) reads as $\epsilon_E = k_z \rho_i^2/r_0$, which is well satisfied for all the values for k_z. The discrepancy due to the absence of electromagnetic effects can be seen in Fig. 3: while the MHD and fully kinetic models are found to be in good agreement for a long-wavelength part of the k-spectra, the COGENT results are systematically lower by 10%–15%.

Compare the impact of the magnetic field variation on the drifts to the main drift term $\mathbf{E} \times \mathbf{B}$. In Eq. (4), the drift term is proportional to $q\nabla\phi + \mu\nabla B$; therefore, parameter $\epsilon_D = \mu\delta B/(q\phi)$ has to be small for the electrostatic approximation to be valid. From Eq. (6), we obtained ϕ as

$$\phi = \delta n \frac{qB^2}{m_i n_i k_z^2 c^2}. \tag{48}$$

Make use of Eqs. (42) and (44) and substitute magnetic moment as $\mu \sim T/B$ to find ϵ_D:

$$\epsilon_D = \frac{k_z r_0 \omega}{\omega_{ci}}. \tag{49}$$

For the ideal MHD mode, $\epsilon_D \sim k_z \rho_i$ and for the entropy mode $\epsilon_D \sim (k_z \rho_i)^2$, so drift corrections are small in the long-wavelength limit and might be considerable otherwise, which is again demonstrated in Fig. 3, as COGENT results start to deviate from PIC ones for $k_z \rho_i \geq 2$.

Finally, as discussed in Sec. III, for the case of $k_z \rho_i \geq 1$, FLR effects become important and therefore have to be treated properly, namely, gyro-orbit averaging, correction of the gyrokinetic Poisson equation, and the pressure term in the expression for density should be included. This motivates us for the next step in code improvement to incorporate all these FLR features, as well as to develop a hybrid MHD-gyrokinetic magnetostatic code. MHD equations are to be used in the region of small magnetic field where the gyrokinetic formalism breaks because the parameter $\epsilon = \omega/\omega_{ci}$ is no longer small. In the region of high plasma magnetization, both codes couple through the pressure term: Gyrokinetics provides a proper pressure tensor for MHD equations and MHD in turn provides time varying magnetic field, and therefore correct drifts for the gyrokinetics. Such an improvement should dramatically increase code applicability and accuracy of the physical model used.

ACKNOWLEDGMENTS

This work was prepared by LLNL for USDOE SC-FES under Contract No. DE-AC52-07NA27344, LLNL LDRD Project No. 18-ERD-007. Special thanks to Kurt Tummel for fruitful discussions and kinetic simulations data.

REFERENCES

[1]P. Reynolds and J. D. Craggs, Philos. Mag. **43**, 258–260 (1952).
[2]I. V. Kurchatov, J. Nucl. Eng. **4**(2), 193–198 (1957).
[3]A. Bishop, *Project Sherwood-The U.S. Program in Controlled Fusion* (Addison-Wesley, Reading, Massachusetts, 1958).
[4]M. G. Haines, Plasma Phys. Controlled Fusion **53**, 093001 (2011).
[5]F. J. Wessel, F. S. Felber, N. C. Wild, H. U. Rahman, A. Fisher, and E. Ruden, Appl. Phys. Lett. **48**, 1119–1121 (1986).
[6]D. D. Ryutov, M. S. Derzon, and M. K. Matzen, Rev. Mod. Phys. **72**, 167–222 (2000).

[7]B. B. Kadomtsev, J. Exp. Theor. Phys. **10**, 780 (1960), see http://www.jetp.ac.ru/cgi-bin/e/index/e/10/4/p780?a=list and the article pdf is this: www.jetp.ac.ru/cgi-bin/dn/e_010_04_0780.pdf.
[8]U. Shumlak, R. P. Golingo, B. A. Nelson, and D. J. D. Hartog, Phys. Rev. Lett. **87**, 205005 (2001).
[9]U. Shumlak, B. A. Nelson, R. P. Golingo, S. L. Jackson, E. A. Crawford, and D. J. D. Hartog, Phys. Plasmas **10**, 1683 (2003).
[10]R. P. Golingo, U. Shumlak, and B. A. Nelson, Phys. Plasmas **12**, 062505 (2005).
[11]U. Shumlak, B. A. Nelson, E. L. Claveau, E. G. Forbes, R. P. Golingo, M. C. Hughes, R. J. Oberto, M. P. Ross, and T. R. Weber, Phys. Plasmas **24**, 055702 (2017).
[12]Y. Zhang, U. Shumlak, B. A. Nelson, R. P. Golingo, T. R. Weber, A. D. Stepanov, E. L. Claveau, E. G. Forbes, and Z. T. Draper, Phys. Rev. Lett. **122**, 135001 (2019).
[13]U. Shumlak and C. W. Hartman, Phys. Rev. Lett. **75**, 3285 (1995).
[14]I. Paraschiv, B. S. Bauer, I. R. Lindemuth, and V. Makhin, Phys. Plasmas **17**, 072107 (2010).
[15]T. D. Arber and D. F. Howell, Phys. Plasmas **3**, 554 (1996).
[16]V. I. Sotnikov, I. Paraschiv, V. Makhin, B. S. Bauer, J. N. Leboeuf, and J. M. Dawson, Phys. Plasmas **9**, 913 (2002).
[17]P. Ricci, B. N. Rogers, and W. Dorland, Phys. Rev. Lett. **97**, 245001 (2006).
[18]P. Ricci, B. N. Rogers, W. Dorland, and M. Barnes, Phys. Plasmas **13**, 062102 (2006).
[19]J. Kesner, A. N. Simakov, D. T. Garnier, P. J. Catto, R. J. Hastie, S. I. Krasheninnikov, M. E. Mauel, T. S. Pedersen, and J. J. Ramos, Nucl. Fusion **41**, 301 (2001).
[20]A. N. Simakov, P. J. Catto, and R. J. Hastie, Phys. Plasmas **8**, 4414 (2001).
[21]A. N. Simakov, R. J. Hastie, and P. J. Catto, Phys. Plasmas **9**, 201 (2002).
[22]A. Navarro, B. Teaca, and F. Jenko, "The anisotropic redistribution of free energy for gyrokinetic plasma turbulence in a Z-pinch," Phys. Plasmas **23**, 042301 (2016).
[23]H. McLean, U. Shumlak, and B. Nelson, in *2016 Exploratory Plasma and Fusion Workshop* (Aubunr, Alabama, 2016).
[24]R. Hazeltine and J. Meiss, *Plasma Confinement* (Courier Corporation, 2003).
[25]M. Coppins, D. J. Bond, and M. G. Haines, Phys. Fluids **27**, 2886 (1984).
[26]K. V. Roberts and J. B. Taylor, Phys. Rev. Lett. **8**, 197–198 (1962).
[27]J. R. Angus, M. Dorf, and V. I. Geyko, "Drift-ideal magnetohydrodynamic simulations of m = 0 modes in Z-pinch plasmas," Phys. Plasmas (submitted).
[28]U. Shumlak, C. S. Adams, J. M. Blakely, B. J. Chan, R. P. Golingo, S. D. Knecht, B. A. Nelson, R. J. Oberto, M. R. Sybouts, and G. Vogman, Nucl. Fusion **49**, 075039 (2009).
[29]K. Tummel, D. P. Higginson, A. J. Link, A. E. W. Schmidt, H. S. McLean, D. T. Offermann, D. R. Welch, R. E. Clark, U. Shumlak, B. A. Nelson, and R. P. Golingo, Phys. Plasmas **26**, 062506 (2019).
[30]M. A. Dorf, R. H. Cohen, M. Dorr, T. Rognlien, J. Hittinger, J. Compton, P. Colella, D. Martin, and P. McCorquodale, Phys. Plasmas **20**, 012513 (2013).
[31]W. H. Bennett, Phys. Rev. **45**, 890 (1934).
[32]W. H. Bennett, Phys. Rev. **98**, 1584 (1955).
[33]E. G. Harris, Nuovo Cimento **23**, 115 (1962).
[34]D. Book, E. Ott, and M. Lampe, Phys. Fluids **19**, 1982 (1976).
[35]M. Dorf, J. Angus, and D. Ghosh, in *The 45th IEEE International Conference on Plasma Science (ICOPS 2018)* (Denver, CO, USA, 2018).